UC Irvine

UC Irvine Previously Published Works

Title

Anisotropic and hierarchical SiC@SiO2 nanowire aerogel with exceptional stiffness and stability for thermal superinsulation

Permalink

https://escholarship.org/uc/item/4t33h7rx

Journal

Science Advances, 6(26)

ISSN

2375-2548

Authors

Su, Lei

Wang, Hongjie

Niu, Min

et al.

Publication Date

2020-06-26

DOI

10.1126/sciadv.aay6689

Copyright Information

This work is made available under the terms of a Creative Commons Attribution License, available at https://creativecommons.org/licenses/by/4.0/

Peer reviewed

eScholarship.org Powered by the California Digital Library
University of California

MATERIALS SCIENCE

Anisotropic and hierarchical SiC@SiO_2 nanowire aerogel with exceptional stiffness and stability for thermal superinsulation

Lei Su[1,2], Hongjie Wang[1]*, Min Niu[1], Sheng Dai[2], Zhixin Cai[1], Biguo Yang[1], Huaixun Huyan[2], Xiaoqing Pan[2]

Copyright © 2020 The Authors, some rights reserved; exclusive licensee American Association for the Advancement of Science. No claim to original U.S. Government Works. Distributed under a Creative Commons Attribution NonCommercial License 4.0 (CC BY-NC).

Ceramic aerogels are promising lightweight and high-efficient thermal insulators for applications in buildings, industry, and aerospace vehicles but are usually limited by their brittleness and structural collapse at high temperatures. In recent years, fabricating nanostructure-based ultralight materials has been proved to be an effective way to realize the resilience of ceramic aerogels. However, the randomly distributed macroscale pores in these architectures usually lead to low stiffness and reduced thermal insulation performance. Here, to overcome these obstacles, a SiC@SiO_2 nanowire aerogel with a nanowire-assembled anisotropic and hierarchical microstructure was prepared by using directional freeze casting and subsequent heat treatment. The aerogel exhibits an ultralow thermal conductivity of ~14 mW/m·K, an exceptional high stiffness (a specific modulus of ~24.7 kN·m/kg), and excellent thermal and chemical stabilities even under heating at 1200°C by a butane blow torch, which makes it an ideal thermally superinsulating material for applications under extreme conditions.

INTRODUCTION

High-efficiency thermal insulators with mechanical robustness and excellent thermal and chemical stabilities are of great significance for safe applications in energy conservation and thermal protection of buildings, industry, and aerospace vehicles (*1*–*4*). As compared to traditional thermal insulators, ceramic aerogels show great advantages owing to their low thermal conductivities (e.g., 12 to 20 mW/m·K of silica aerogels) and good chemical stability (e.g., fire and corrosion resistance) (*5*–*9*). However, the brittle nature of ceramics and structural collapse at high temperatures impose limitations on wide applications of the conventional ceramic aerogels that are composed of oxide nanoparticles (*10*–*13*). Some of the emerging recoverable graphene aerogels are highlighted owing to their thermal insulation, such as naturally dried graphene aerogel (18 mW/m·K in air) (*14*), aminosilane–cross-linked graphene aerogels (19 mW/m·K in air) (*15*), and three-dimensional graphene scaffolds (12.6 mW/m·K in vacuum) (*16*). However, because of the decomposition behavior of graphene-based materials at temperatures higher than 600°C (*14*), they are hardly to be used under high-temperature and oxygen-containing conditions.

To overcome these drawbacks, recent efforts have been made in the fabrication of highly porous ceramic architectures assembled by flexible yet robust ceramic nanostructures. This class of materials, such as BN aerogels (*17*), BN foams (*18*), oxide nanofiber sponges (*19*), SiC nanowire aerogel (*20*), SiO_2 nanofiber aerogel (*21*), and Si_3N_4 nanobelt aerogel (*22*), has realized large-strain resilient compressibility. In addition, the use of carbide (*20*) or nitride (*17*, *18*, *22*) constituents in some of these materials also brings them improved thermal stability. However, these modified materials usually have a microstructure with nanofiber-assembled randomly distributed macroscale pores, which cannot efficiently reduce heat conduction like nanoparticle-assembled ceramic aerogels, thus leading to a higher thermal conductivity than that of the conventional silica aerogels, and their relative low stiffness (a specific modulus lower than 5 kN·m/kg) would hinder the ways for their practical applications (*4*, *19*–*21*).

Previous studies have shown that highly porous materials with an anisotropic honeycomb microstructure can simultaneously achieve improved mechanical properties and thermal insulation (*2*, *23*–*25*). On one hand, cell walls of the aligned tubular pores in the honeycomb structure serve as ribs to enhance the mechanical performance in the pore alignment direction, leading to enhanced modulus and strength (*2*, *23*, *24*).On the other hand, the anisotropic microstructure gives rise to anisotropic thermal conductivity, which would help reduce heat transfer in the direction with lower thermal conductivity through increasing heat flow in the direction with higher thermal conductivity, resulting in improved thermal insulation performance (*2*, *23*).

It has also shown that the solid heat conduction of materials can be substantially reduced through introducing a large amount of phonon barriers in nanostructures (*26*–*28*), such as Ge multilayer nanodot in a single-crystalline SiGe material (*29*), amorphous SiO_2 shell on the surface of silicon nanowires (*30*), and stacking faults in SiC nanowires (*31*). For SiC nanowire, in addition to high mechanical robustness, good flexibility, and excellent thermal and chemical stabilities (*19*, *32*, *33*), there are usually a large amount of phonon barriers introduced during its growth and subsequent treatment process, i.e., dense distribution of stacking faults along the nanowire length and an amorphous SiO_2 shell on the surface of each nanowire.

Here, inspired by these ideas, we choose SiC nanowires as building blocks to construct ultralight ceramic aerogel by using a controlled directional freeze casting and a subsequent heat treatment process (Fig. 1, A and B). Introduction of a SiO_2 shell on the surface of a SiC nanowire during the subsequent heat treatment results in the formation of well-interconnected junctions and the establishment of multiscale thermal conducting barriers in the architecture of the obtained SiC-SiO_2 core-shell (SiC@SiO_2) nanowire aerogel. The SiC@SiO_2 nanowire aerogel exhibits an anisotropic and hierarchical

[1]State Key Laboratory for Mechanical Behavior of Materials, Xi'an Jiaotong University, Xi'an 710049, P. R. China. [2]Department of Materials Science and Engineering, University of California, Irvine, Irvine, CA 92697, USA.
*Corresponding author. Email: hjwang@xjtu.edu.cn

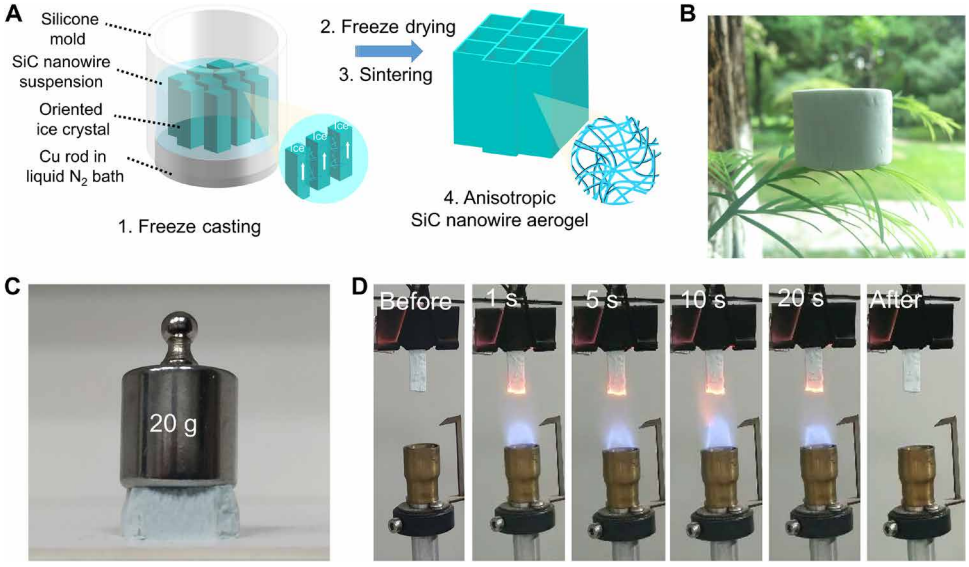

Fig. 1. Fabrication process and overview of the mechanical performance and fire resistance of the AH-SSCSNWA. (**A**) Fabrication process of the AH-SSCSNWA. (**B**) Photograph of a piece of the AH-SSCSNWA with a volume of ~15 cm^3, standing on a leaf, indicating its ultralow density. (**C**) Photograph showing that a 20-g weight can be supported by a piece of the AH-SSCSNWA with a weight of 5 mg, demonstrating the high stiffness of the AH-SSCSNWA. (**D**) Vertical burning test showing the good fire resistance of the AH-SSCSNWA. Photo credit: Lei Su, Xi'an Jiaotong University.

microstructure where assembled into aligned tubular pores. Thus, the aerogel is referred to as "AH-SSCSNWA." The multiscale thermal conducting barriers in the aerogel enable it an ultralow thermal conductivity of ~14 mW/m·K in radial direction (perpendicular to the pore alignment direction). The anisotropic microstructure with aligned tubular pores also results in an unusual stiffness (a high specific modulus of 24.7 kN·m/kg) in the axial direction (pore alignment direction), which makes a piece of the aerogel able to support over 4000 times its own weight without any visible damage (Fig. 1C). The use of all ceramic constituents guarantees the AH-SSCSNWA excellent thermal and chemical stabilities in oxygen-containing environment, such as the good fire resistance demonstrated by the vertical burning test (Fig. 1D).

RESULTS

Fabrication and structure characterization

Freeze drying, which has been proved to be an efficient way to construct anisotropic and highly porous architectures (*2*, *34*, *35*), was used here to fabricate the anisotropic and hierarchical SiC scaffold. SiC nanowires with a diameter of 20 to 50 nm and a length of up to several micrometers were used as the raw materials. They were dispersed in deionized water, and a uniform and stable suspension (fig. S1) was obtained by mechanical stirring. During the directional freeze casting, the SiC nanowire suspension was poured into a silicone mold installed on the top of a copper rod (Fig. 1A and fig. S2). The copper rod was cooled by liquid N_2, and its top surface was controlled at a constant temperature of −90°C. Because of the large temperature gradient between the cooper rod and suspension, oriented growth of ice crystals took place. As a result, the suspended SiC nanowires were pushed into the ice crystal boundaries, forming a frozen composite consisting of oriented ice crystals with surrounded SiC nanowire walls. Afterward, the ice crystal template was removed by freeze drying, forming a self-supporting SiC nanowire scaffold with aligned microscale pores. Notably, the scaffold was not robust enough at this stage because of the lack of strong interaction between the nanowires. Therefore, additional air annealing of the scaffold was performed at 1000°C for 20 min, during which SiC nanowires were partially oxidized to form a thin and amorphous SiO_2 shell on the nanowire surface (details of the manipulation of the thickness of the amorphous SiO_2 shell are presented in fig. S3). Therefore, this kind of nanostructure is named as "SiC@SiO_2 nanowire." The adjacent nanowires were fused together by the oxide layers after this treatment (Fig. 2G), resulting in the AH-SSCSNWA with a well-interconnected architecture. Densities of the samples can be adjusted by using SiC nanowire suspension with different concentrations. In the present work, we have prepared AH-SSCSNWA with densities ranging from 1.4 to 6.5 mg/cm^3 by using ranging suspensions, with concentrations ranging from 1.5 to 7 mg/ml. The microstructure and properties of AH-SSCSNWA were investigated by using the sample with a density of 6.5 mg/cm^3, except as otherwise noted.

Figure 1B shows a piece of the AH-SSCSNWA with a volume of ~15 cm^3 being supported by a leaf, highlighting its ultralow density, making it one of the superlight ceramics (*4*, *18*–*22*, *36*, *37*). Scanning electron microscopy (SEM) and transmission electron microscopy (TEM) were used to characterize microstructure and compositions of the AH-SSCSNWA. As displayed in Fig. 2 (A to G), it is revealed that the aerogel exhibits an anisotropic and hierarchical microstructure where the nanowires assemble and form aligned tubular pores. The cross-sectional area of the pores is about 625 μm^2 in average where the side length is about 25 μm (Fig. 2A). Notably, the pores are connected with each other through the interweaving nanowires at triangular junctions (Fig. 2B). An additional side view in Fig. 2D shows that the length of the tubular pores can be more than several millimeters, arranging along the ice growth direction throughout the whole material. The cell walls are assembled by thousands of SiC@SiO_2 nanowires (Fig. 2C), which were fused together through the amorphous SiO_2 shell at a nanometer level

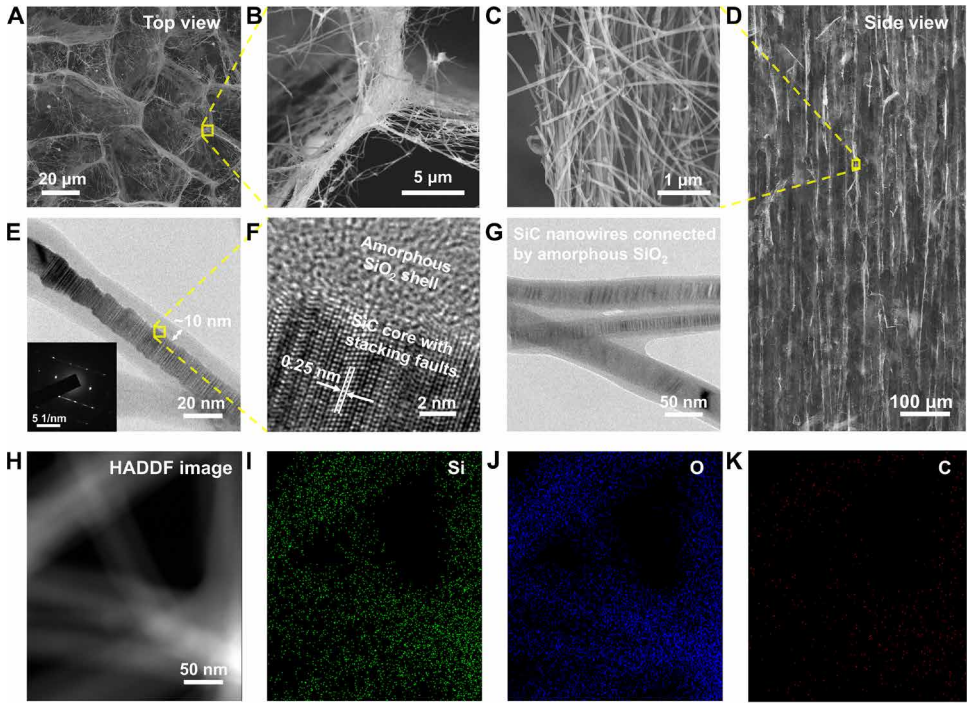

Fig. 2. Structure characterization of the AH-SSCSNWA. (**A** and **D**) Microstructure of the AH-SSCSNWA from top and side views, respectively. (**B** and **C**) Magnified images of the marked areas in (C) and (F), respectively. (**E**) TEM image of the SiC@SiO_2 nanowire, inset presenting the corresponding selected-area electron diffraction pattern. (**F**) High-resolution TEM image of the SiC@SiO_2 nanowire. (**G**) TEM microstructure showing the SiO_2 conjunction between nanowires. (**H**) High-angle annular dark-field (HAADF) image. (**I** to **K**) The corresponding EDS mapping of the SiC@SiO_2 nanowire.

(Fig. 2G). With the increase of sample densities from 1.4 to 6.5 mg/cm^3, the cell wall became denser, showing an evolution of the microstructure with the variation of sample densities (fig. S4). The 3C-SiC core with densely distributed stacking faults along the nanowire length and an amorphous SiO_2 shell on the surface of the nanowire were verified by the selected-area electron diffraction (inset in Fig. 2E) pattern, high-resolution TEM image (Fig. 2F), and energy-dispersive spectroscopy (EDS; Fig. 2, I to K). These stacking faults and amorphous interfaces could act as phonon barriers to reduce solid conduction in the aerogels' architecture (*27*, *30*, *31*).

Thermal superinsulation performance

Heat-transfer behavior in the AH-SSCSNWA was first investigated by observation of the heat flow along the radial and axial direction, respectively. As displayed in Fig. 3 (A and B), a 4-mm spot-size laser (a radiation wavelength of 1064 nm and an intensity of 8 W/mm^2) was applied along the two directions of a piece of AH-SSCSNWA (with a diameter of 50 mm and a thickness of 10 mm). Along the axial direction, heat transfer through the 10-mm-thick AH-SSCSNWA within 0.37 s. After 0.4 s, a spot with 4 mm in diameter with the temperature of up to 98°C formed (Fig. 3A and movie S1). In contrast, along the radial direction, it needs 1 s to reach the maximum temperature (98°C) at a position of 10-mm distance from the surface. After an elapsed time of 1 s, the temperature profile became stable and remained almost the same in the following 120 s, indicating good thermally insulating performance in the radial direction (Fig. 3B and movie S2). The different heat transfer behaviors along the two main directions confirm anisotropy of the thermal conductivity, which is similar to those of other anisotropic thermal insulators in the reported literatures (*2*, *23*).

As shown in Fig. 3C and table S1, the thermal conductivities are measured to be about 14 and 35 mW/m·K along the radial and axial direction, respectively, giving an anisotropic factor of ~2.5. This obvious anisotropy is consistent with the observed heat transfer behavior. Particularly, the thermal conductivity value in the radial direction is comparable to that of the reported thermally superinsulating materials, such as anisotropic cellulose/graphene oxide foam (*2*), BN aerogel (*4*), and silica aerogel (*5*), highlighting thermal superinsulation performance of the AH-SSCSNWA.

Specifically, the radial thermal conductivity of the AH-SSCSNWA is two times lower than that of the SiC nanowire aerogel (26 mW/m·K) with randomly distributed microstructure (*20*), demonstrating the superiority of the anisotropic and hierarchical structural design. In addition, as compared to other anisotropic thermal insulators, for example, the SiC microwhisker networks (approximately 100 mW/m·K in the radial direction) with a porosity of 98%, the AH-SSCSNWA shows an enhanced thermal insulation performance up to eightfold higher in the radial direction (*37*). This result demonstrates the advantage of nanosized building blocks (SiC@SiO_2 nanowires) with large amounts of phonon barriers.

As is known, conduction, convection, and radiation are three ways for thermal conducting. Because of the relative low testing temperature (e.g., room temperature), radiation is negligible (*7*). Thus, in the AH-SSCSNWA, solid conduction, gas conduction, and gas convection mainly contribute to its thermal conductivity. At the macroscale, the AH-SSCSNWA (density of 6.5 mg/cm^3) is composed of ~99.8 volume percent (volume %) pores and only ~0.2 volume % solid constituent where solid conduction is limited. At the microscale, the aligned pores serve as channels for gas convection, while the aligned tube walls serve as channels for solid conduction in axial directions, which would

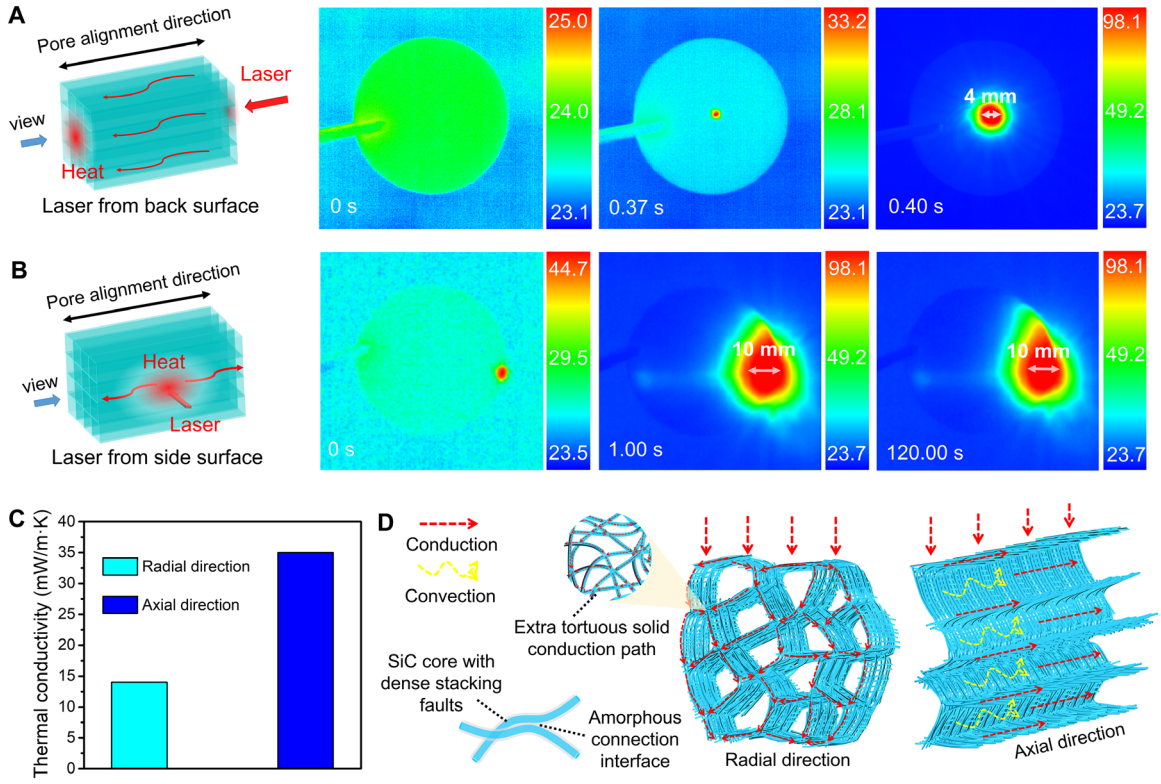

Fig. 3. Thermal superinsulation performance of the AH-SSCSNWA. Thermal conducting behavior of the AH-SSCSNWA in the (**A**) axial and (**B**) radial directions, respectively, showing the anisotropic heat transfer behavior in different directions. (**C**) The thermal conductivities of the AH-SSCSNWA in axial and radial directions. (**D**) A schematic illustration showing the mechanism to achieve thermal superinsulation.

increase the heat transfer in axial direction and thus reduce thermal conductivity in radial direction (Fig. 3D). In addition, as shown in the inset in Fig. 3D, the pore structure and the use of nanowire building blocks bring a large amount of extra tortuous solid conduction paths in the cross section, slowing down the heat transfer efficiency in radial direction. At the nanoscale, the use of nanowire building blocks brings large amount of phonon barriers (the amorphous SiO_2 interface between adjacent nanowires and the stacking faults in the SiC core, Fig. 3D), resulting in increased interfacial thermal resistance and thus reduced solid conduction. Together, these four main factors in the three size scales synergistically produce thermal superinsulation in the AH-SSCSNWA.

High stiffness in the axial direction

Anisotropic and hierarchical structural design is also thought to be beneficial to the improvement of the mechanical properties of the AH-SSCSNWA. Here, a quasi-static compression test was performed, and distinct deformation behaviors were observed along the axial and radial directions. Specifically, the aerogel exhibits a stiff deformation behavior in the axial direction. The compression stress-strain (σ-ε) curve in Fig. 4A shows four deforming stages: a linear elastic regime <2.5% strain, a nonlinear elastic regime between 2.5 and 7% strain, a plastic yielding plateau between 7 and 48% strain, and a densification process after 48% strain. The compression modulus (E) calculated from the linear elastic regime is about 160.8 kPa, yielding a specific modulus (E/ρ) of ~24.7 kN·m/kg, which is significantly higher than those of many other ultralight materials with a random microstructure (Fig. 4B) (*4*, *19*, *20*, *21*).

With the increase of sample densities, the relative modulus shows obvious improvement (Fig. 4C and fig. S5), which is attributed to the denser cell wall of the aligned tubular pores (fig. S4). The relative modulus E/E_s over the relative density ρ/ρ_s is plotted in Fig. 4D. It is clear that the AH-SSCSNWA is located on the dash line, displaying a quadratic relationship (*22*, *38*, *39*), i.e., $E/E_s = (\rho/\rho_s)^2$. This relationship indicates a bending-dominated deformation mechanism and robust connections between the building blocks (*39*, *40*, *41*). Intriguingly, by measuring size changes during compression (Fig. 4E and movie S3), it can be found that the aerogel exhibits a negative Poisson's ratio of ~−0.08 in the axial direction, which represents an unusual mechanical enhancement of rib-like nanowire–assembled walls (*4*, *42*–*44*).

The deformation process of the AH-SSCSNWA was investigated by an in situ SEM mechanical test. It is revealed that the aligned tubular walls show a local buckling deformation under compression (Fig. 4E). After the load was released, the buckled tubular walls returned to their original state, verifying their desirable flexibility and robustness. This deformation behavior of the tubular walls is related to the elastic region in the strain-stress curve. Furthermore, a successive loading-unloading compression test was carried out up to five cycles and 30% strain to illustrate mechanical robustness of the tube wall (Fig. 4E), during which the modulus and yield strength were almost the same (fig. S6). In addition, the zigzag appeared in the successive compression stress-strain curves after 7% compression strain (Fig. 4F), indicating the mechanical energy loss during the plastic deformation stage. This might be related to the cracking of the cell walls. Further increase of the compression strain resulted

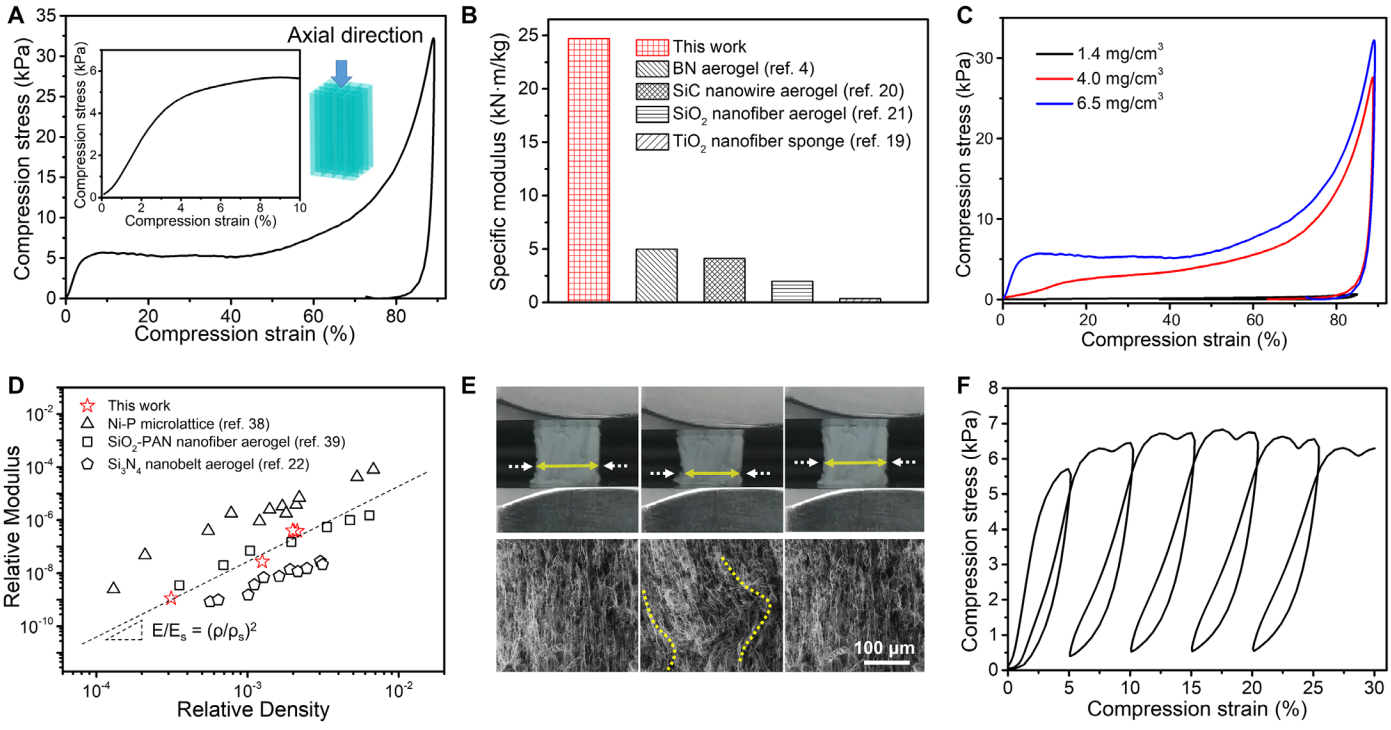

Fig. 4. Mechanical performance of the AH-SSCSNWA in the axial direction. (**A**) Compression stress-strain curve of the AH-SSCSNWA in the axial direction showing four deformation regions: a linear elastic regime <2.5% strain, a nonlinear elastic regime between 2.5 and 7% strain, a plastic yielding plateau between 7 and 48% strain, and a densification process after 48% strain. The inset shows the amplified curve in the strain range of 0 to 50%. (**B**) Comparison of the specific modulus of the AH-SSCSNWA with those of other aerogels with random structure. (**C**) Mechanical properties of AH-SSCSNWA with densities ranging from 1.4 to 6.5 mg/cm^3 in the axial direction. (**D**) Relative Young's modulus of different highly porous architectures plotted over their relative density. (**E**) Structure evolution of the AH-SSCSNWA in the elastic compression region in the axial direction. (**F**) Successive unloading-reloading compression test of the AH-SSCSNWA in the axial direction.

in the damage of the sample structure, leading to the fracture of the sample after 90% compression strain (fig. S7).

Reversible compressibility in the radial direction

Unlike the stiff behavior in the axial direction, the AH-SSCSNWA shows mechanical flexibility in the radial direction. Similar to the high compressibility of other isotropic ceramic aerogels with randomly oriented flexible building blocks (*17*–*19*, *21*), the AH-SSCSNWA can recover to its original configuration from 80% strain after releasing in the axial direction (Fig. 5A). Three distinctive regimes were observed in the loading process: a linear elastic region below 12% strain, a nearly plateau regime between 12 and 60% strain, and a nonlinear elastic regime with rapidly increasing modulus after 60% strain. The modulus in the linear elastic region is calculated to be 10.6 kPa, only $^1/_{16}$ of that in the axial direction, demonstrating the high anisotropy of the AH-SSCSNWA again. Similar to the deformation behavior in the axial direction, with the increase of the sample densities from 1.4 to 6.5 mg/cm^3, the compression strain-stress curves in the radial direction also show an increase of the modulus and compression stress (Fig. 5B). In situ SEM observation of the structure evolution during compression shows that the recoverable compressibility is achieved through the elastic bending of the tube walls (Fig. 5C). The triangle junction between neighboring tubular pores worked as the fulcrum of the elastic bending and remained well during the compression (Fig. 5C). Moreover, this resilient compressibility shows a durable cycling performance even at a high strain rate of 80 mm/min at a set strain of 60% (Fig. 5D and movie S4). After 100 cycles, no obvious change was observed in the relative height of the sample (Fig. 5E). The maximum stress decreased during the first 20 cycles but remained almost constant after the 20th cycle (Fig. 5F). These observations highlight the good structure stability of AH-SSCSNWA under a cyclic fatigue test.

Thermal and chemical stabilities

Thermal and chemical stabilities are another critical criterion to evaluate application safety of thermal insulators. The good thermo-oxidative stability was illustrated by isothermal treatment at 1000°C in an air furnace. After the sample was treated for 30 min or longer, no obvious change was observed in the macroscopic morphology (Fig. 6A). Figure 6 (B and C) shows the compression stress-strain curves of the sample after isothermal treatment at 1000°C for 30 min. By comparison, it shows a ~20% increase of the stress in the plastic yielding plateau in the axial stress-strain curve (fig. S8). This increase might be a result from the increased thickness of the amorphous SiO_2 layer (inset in Fig. 6B). The thicker amorphous SiO_2 layer could result in better junctions between neighboring nanowires. The AH-SSCSNWA aerogel was further subjected to a butane blow torch (Fig. 6D) to simulate an erosion environment where the maximum temperature is higher than 1200°C (Fig. 6E). Notably, the macroscopic morphology remained almost the same after being treated for more than 30 min (Fig. 6F), except for some surface ablation traces observed in the SEM image (Fig. 6G). This excellent erosion

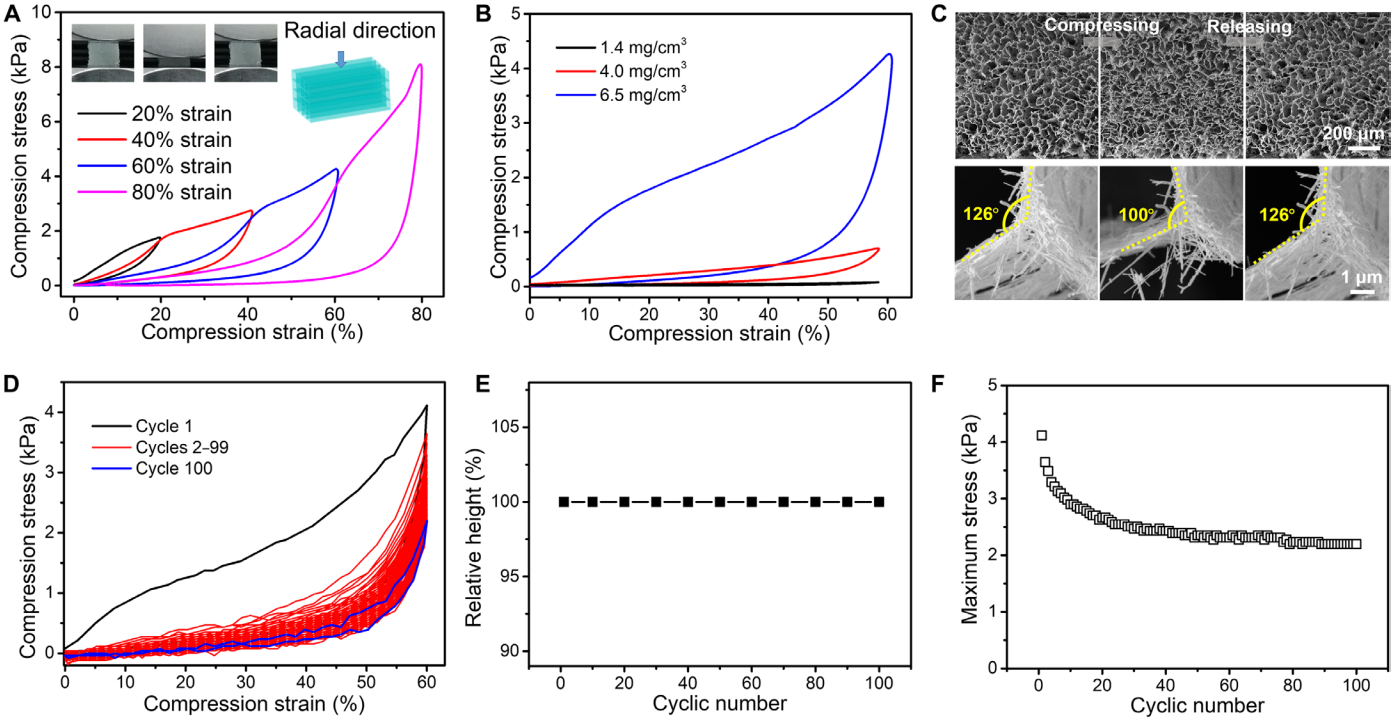

Fig. 5. Mechanical performance of the AH-SSCSNWA in the radial direction. (**A**) Compression stress-strain curve of the AH-SSCSNWA in the radial direction, showing high compressibility. (**B**) Mechanical properties of AH-SSCSNWA with densities ranging from 1.4 to 6.5 mg/cm^3 in the radial direction. (**C**) Structure evolution of the AH-SSCSNWA during the compressing and releasing process in the radial direction. (**D**) One hundred cyclic compression stress-strain curves of the AH-SSCSNWA in the radial direction. (**E**) Relative height evolution during 100 compression cycles. (**F**) Maximum stress evolution during 100 compression cycles.

resistance gives the AH-SSCSNWA the ability to recover from repeated compression in the radial direction at 1200°C under heating by a butane blow torch (Fig. 6H and movie S5).

Such good thermal-oxidation and erosion resistance is mainly attributed to the superior chemical stability of the SiC@SiO_2 nanowires, which was further verified by thermogravimetric analysis (TGA) in air. As shown in Fig. 6I, the weight of AH-SSCSNWA sample remained stable up to 900°C, indicating its good thermo-oxidative stability. From 900° to 1000°C, it shows a 2% weight gain. After 1000°C, the weight gain rate became stable. The weight gain is due to oxidation of the SiC core, demonstrated by the increased thickness of the amorphous SiO_2 layer observed in the TEM images after isothermal treatment (an increase of ~10 nm, inset in Fig. 6B) and heat treatment by the butane blow torch (an increase of ~15 nm, Fig. 6J). It could be also verified by the decreased Si-C peak at 779/cm and increased Si-O peaks at 457 and 1078/cm in the Fourier transform infrared (FTIR) spectra (Fig. 6K) of the sample after heat treatment by the butane blow torch. The increased amorphous oxide layer could protect the nanowire from further oxidation through slowing down the diffusion rate of oxygen.

For comparison, the AH-SSCSNWA has integrated properties of ultralow thermal conductivity and excellent thermal and chemical stabilities (1000°C under air conditions and 1200°C in fire-erosion environment) that are superior to traditional polymeric thermal insulators (*1*), fiberglass wool (*1*), commercial silica aerogel and its composites (*9*, *20*), and other recently reported resilient ceramic aerogels (*4*, *20*, *21*, *22*) (Fig. 6L), highlighting its potential for applications in high-temperature and oxygen-containing environments, such as fire-proofing thermal insulator for buildings and thermal protecting materials for aerospace vehicles.

DISCUSSION

In summary, we have fabricated an anisotropic and hierarchical SiC@SiO_2 nanowire aerogel with nanowire-assembled aligned tubular pores by using a controlled directional freeze-casting method, combined with a subsequent heat treatment process. The aerogel displays a combination of outstanding properties, including radial thermal superinsulation (14 mW/m·K), recoverable radial compressibility (repeated full recovery from 80% strain), exceptional axial stiffness (a specific modulus of 24.7 kN·m/kg), and good thermal and chemical stabilities (even stable at 1200°C in oxygen-containing environment). The ultralow thermal conductivity is benefited from the rationally designed multiscale thermal barriers. The high axial-specific modulus, which is ~5 times higher than that of other resilient ceramic aerogels, mainly results from the unusual enhancement of the flexible yet robust aligned tubular pore walls. The excellent thermal and chemical stabilities are attributed to the chemical stability of its carbide ceramic nature. These integrated properties ensure the aerogel as a promising thermal insulation material for safe applications in extreme environment, especially under high-temperature and oxygen-containing conditions where conventional polymeric insulating materials are easily ignited and ceramic nanoparticle-based aerogels are usually collapsed. Design and fabrication of such an intriguing ceramic aerogel provide substantial motivation for the development of other high-performance nanostructure-based materials.

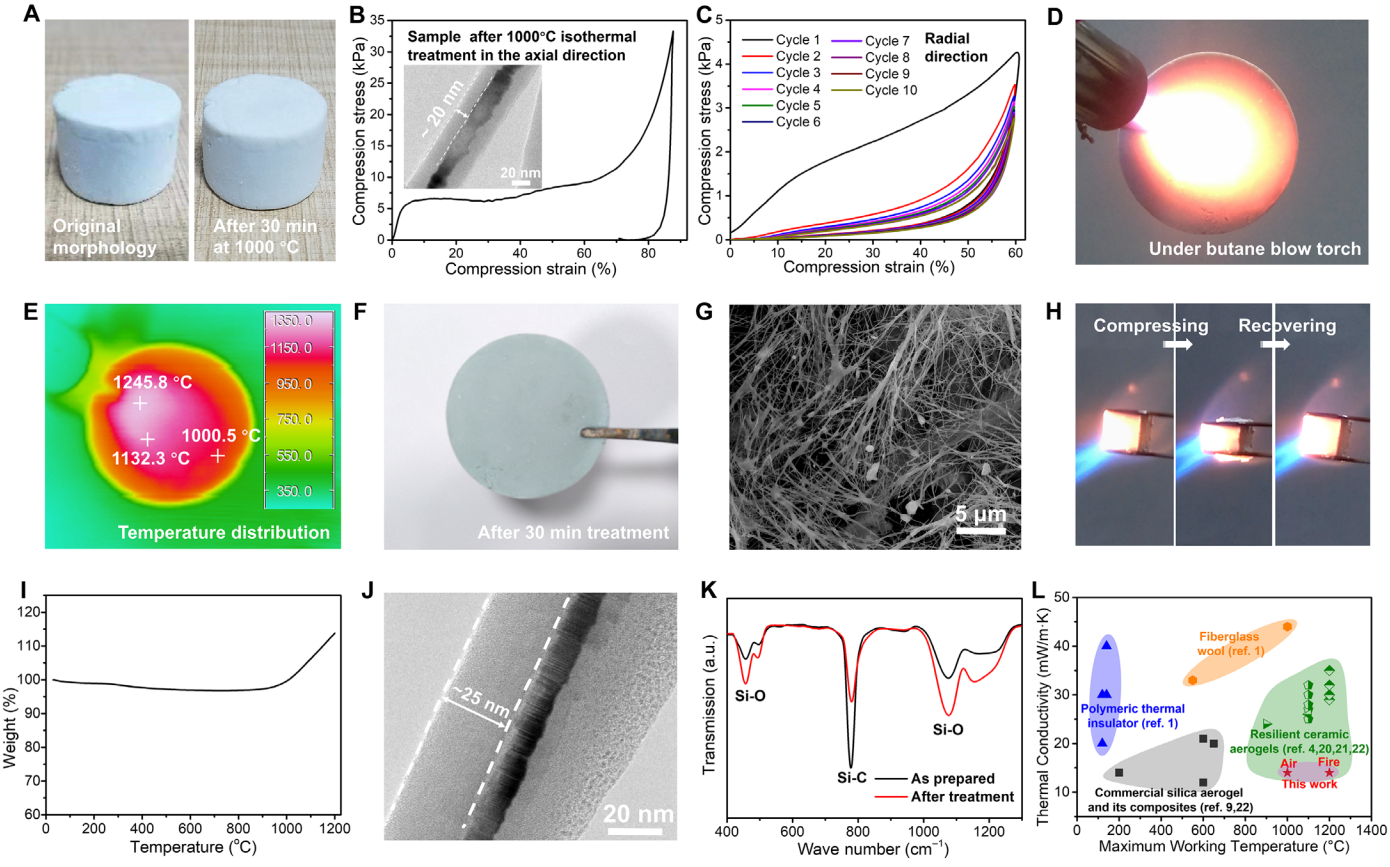

Fig. 6. Fire and high-temperature resistance of the AH-SSCSNWA. (**A**) Macroscopic morphologies of a piece of AH-SSCSNWA before and after isothermal treatment in an air furnace at 1000°C for 30 min. (**B** and **C**) Compression stress-strain curves of the AH-SSCSNWA after isothermal treatment at 1000°C for 30 min in the axial and radial directions, respectively. The inset in Fig. 6B shows the TEM image of the nanowire after isothermal treatment at 1000°C for 30 min. (**D**) A piece of the AH-SSCSNWA under the heating of a butane blow torch. (**E**) Temperature distribution on the surface of the aerogel detected by using an infrared camera. (**F**) Photograph of the aerogel after being treated by the butane blow torch for 30 min. (**G**) SEM of the aerogel after being treated by the butane blow torch for 30 min. (**H**) Repeated compression-recovery ability of the aerogel under butane blow torch. (**I**) TGA curve of the aerogel obtained in air atmosphere. (**J**) TEM image of the nanowire after being treated by the butane blow torch for 30 min. (**K**) FTIR spectra of the aerogel before and after the butane blow torch treatment for 30 min. (**L**) Maximum working temperature of thermal insulators in oxygen-containing environment. Photo credit: Lei Su, Xi'an Jiaotong University. a.u., arbitrary units.

MATERIALS AND METHODS

Preparation of SiC nanowire suspension

SiC nanowires with a diameter of 20 to 50 nm were prepared by chemical vapor deposition as we previously reported (*20*). To prepare the AH-SSCSNWA with a density of 6.5 mg/cm^3, 350 mg of SiC nanowires was dispersed in 50 ml of deionized water by mechanical stirring at 1000 rpm for 8 hours to obtain a homogeneous nanowire suspension with a concentration of 7 mg/ml (fig. S1). The suspension concentration used in the present work ranges from 1.5 to 7 mg/ml.

Characterization

The vertical burning test of the AH-SSCSNWA was conducted by using a vertical burning tester (ZR-02, Qingdao, China). The microstructure of the AH-SSCSNWA was characterized by SEM (Quanta 600, FEI, USA), TEM (JEM-2100, JEOL, Japan), and scanning TEM (STEM, JEM-ARM300CF, JEOL, Japan). The elemental compositions were detected by EDS equipped on the STEM. FTIR spectrum (VERTEX70, Bruker, Germany) was used to characterize the chemical bond of the nanowire. The density of AH-SSCSNWA was calculated from mass and geometry of the samples. The quasi-static compression tests were conducted using a TA-Q800 DMA instrument at 2 mm/min. The 100 cyclic loading-unloading fatigue test in the radial direction of AH-SSCSNWA was conducted using an Instron 5943 testing system at 80 mm/min. In situ observation of microstructure evolution during compression was performed in the SEM. The fire resistance was characterized by subjecting the AH-SSCSNWA to a butane blow torch, and the corresponding infrared image was recorded by a thermal infrared imager (NEC, TH5100, Japan) to illustrate surface temperature distribution. TGA was performed with a TGA thermal analyzer (TGA/DSC3+, Mettler Toledo, Switzerland) from room temperature to 1200°C in air at a heating rate of 10°C/min.

Thermal conductivity test

An AH-SSCSNWA sample with the diameter of 50 mm (radial direction) and the thickness of 10 mm (axial direction) was used for the investigation of the anisotropic heat-conducting behavior in ambient air at room temperature. A laser at a 1064-nm radiation wavelength with an intensity of 8 W/ mm^2 and a spot size of 4 mm was applied in the axial and radial directions, respectively. An infrared

camera (FLIR SC6700, FLIR System, USA) was used to record the heat-conducting process in the radial and axial direction. Thermal conductivities in the axial and radial directions were measured by a Laser flash apparatus (LFA467, Netzsch, Germany) at room temperature in air, according to previous literatures (*25*, *36*, *45*). The thermal conductivity was calculated by Eq. 1

$$\kappa = \alpha\rho C_p \quad (1)$$

where κ is the calculated thermal conductivity, α is the measured thermal diffusivity, ρ is the density of the AH-SSCSNWA, and C_p is the specific heat capacity. The C_p is measured by a differential scanning calorimetry method (DSC 204 F1 Phoenix, NETZSCH, Germany). The detail results are presented in table S1.

SUPPLEMENTARY MATERIALS

Supplementary material for this article is available at http://advances.sciencemag.org/cgi/content/full/6/26/eaay6689/DC1

REFERENCES AND NOTES

1. B. P. Jelle, Traditional, state-of-the-art and future thermal building insulation materials and solutions – Properties, requirements and possibilities. *Energ. Buildings* **43**, 2549–2563 (2011).
2. B. Wicklein, A. Kocjan, G. Salazar-Alvarez, F. Carosio, G. Camino, M. Antonietti, L. Bergström, Thermally insulating and fire-retardant lightweight anisotropic foams based on nanocellulose and graphene oxide. *Nat. Nanotechnol.* **10**, 277–283 (2015).
3. N. Bheekhun, A. R. Abu Talib, M. R. Hassan, Aerogels in aerospace: An overview. *Adv. Mater. Sci. Eng.* **2013**, 406065 (2013).
4. X. Xu, Q. Zhang, M. Hao, Y. Hu, Z. Lin, L. Peng, T. Wang, X. Ren, C. Wang, Z. Zhao, C. Wan, H. Fei, L. Wang, J. Zhu, H. Sun, W. Chen, T. Du, B. Deng, G. J. Cheng, I. Shakir, C. Dames, T. S. Fisher, X. Zhang, H. Li, Y. Huang, X. Duan, Double-negative-index ceramic aerogels for thermal superinsulation. *Science* **363**, 723–727 (2019).
5. M. Koebel, A. Rigacci, P. Achard, Aerogel-based thermal superinsulation: An overview. *J. SolGel Sci. Technol.* **63**, 315–339 (2012).
6. T. Kashiwagi, F. Du, J. F. Douglas, K. I. Winey, R. H. Harris Jr., J. R. Shields, Nanoparticle networks reduce the flammability of polymer nanocomposites. *Nat. Mater.* **4**, 928–933 (2015).
7. Z.-L. Yu, N. Yang, V. Apostolopoulou-Kalkavoura, B. Qin, Z. Y. Ma, W. Y. Xing, C. Qiao, L. Bergström, M. Antonietti, S.-H. Yu, Fire-retardant and thermally insulating phenolic-silica aerogels. *Angew. Chem. Int. Ed.* **57**, 4538–4542 (2018).
8. A. C. Pierre, G. M. Pajonk, Chemistry of aerogels and their applications. *Chem. Rev.* **102**, 4243–4265 (2002).
9. N. Hüsing, U. Schubert, Aerogels—Airy materials: Chemistry, structure, and properties. *Angew. Chem. Int. Ed.* **37**, 22–45 (1998).
10. B. M. Novak, D. Auerbach, C. Verrier, Low-density, mutually interpenetrating organic-inorganic composite materials via supercritical drying techniques. *Chem. Mater.* **6**, 282–286 (1994).
11. N. Leventis, C. Sotiriou-Leventis, G. Zhang, A. M. Rawashdeh, Nanoengineering strong silica aerogels. *Nano Lett.* **2**, 957–960 (2002).
12. A. Emmerling, J. Gross, R. Gerlach, R. Goswin, G. Reichenauer, J. Fricke, H.-G. Haubold, Isothermal sintering of SiO_2-aerogels. *J. Non Cryst. Solids* **125**, 230–243 (1992).
13. R. Saliger, T. Heinrich, T. Gleissner, J. Fricke, Sintering behavior of alumina-modified silica aerogels. *J. Non Cryst. Solids* **186**, 113–117 (1995).
14. X. Xu, Q. Zhang, Y. Yu, W. Chen, H. Hu, H. Li, Naturally dried graphene aerogels with superelasticity and tunable Poisson's ratio. *Adv. Mater.* **28**, 9223–9230 (2016).
15. G. Zu, K. Kanamori, K. Nakanishi, X. Lu, K. Yu, J. Huang, H. Sugimura, Superelastic multifunctional aminosilane-crosslinked graphene aerogels for high thermal insulation, three-component separation, and strain/pressure-sensing arrays. *ACS Appl. Mater. Interfaces* **11**, 43533–43542 (2019).
16. Q. Zhang, M. Hao, X. Xu, G. Xiong, H. Li, T. S. Fisher, Flyweight 3D graphene scaffolds with microinterface barrier-derived tunable thermal insulation and flame retardancy. *ACS Appl. Mater. Interfaces* **9**, 14232–14241 (2017).
17. G. Li, M. Zhu, W. Gong, R. Du, A. Eychmüller, T. Li, W. Lv, X. Zhang, Boron nitride aerogels with super-flexibility ranging from liquid nitrogen temperature to 1000°C. *Adv. Funct. Mater.* **29**, 1900188 (2019).
18. J. Yin, X. Li, J. Zhou, W. Guo, Ultralight three-dimensional boron nitride foam with ultralow permittivity and superelasticity. *Nano Lett.* **13**, 3232–3236 (2013).
19. H. Wang, X. Zhang, N. Wang, Y. Li, X. Feng, Y. Huang, C. Zhao, Z. Liu, M. Fang, G. Ou, H. Gao, X. Li, H. Wu, Ultralight, scalable, and high-temperature-resilient ceramic nanofiber sponges. *Sci. Adv.* **3**, e1603170 (2017).
20. L. Su, H. Wang, M. Niu, M. Ma, X. Fan, Z. Shi, S.-W. Guo, Ultralight, recoverable, and high-temperature-resistant SiC nanowire aerogel. *ACS Nano* **12**, 3103–3111 (2018).
21. S. Yang, X. Wang, L. Dou, J. Yu, B. Ding, Ultralight and fire-resistant ceramic nanofibrous aerogels with temperature-invariant superelasticity. *Sci. Adv.* **4**, eaas8925 (2018).
22. L. Su, M. Li, H. Wang, M. Niu, D. Lu, Z. Cai, Resilient Si_3N_4 nanobelt aerogel as fire-resistant and electromagnetic wave-transparent thermal insulator. *ACS Appl. Mater. Interfaces* **11**, 15795–15803 (2019).
23. T. Li, J. Song, X. Zhao, Z. Yang, G. Pastel, S. Xu, C. Jia, J. Dai, C. Chen, A. Gong, F. Jiang, Y. Yao, T. Fan, B. Yang, L. Wågberg, R. Yang, L. Hu, Anisotropic, lightweight, strong, and super thermally insulating nanowood with naturally aligned nanocellulose. *Sci. Adv.* **4**, eaar3724 (2018).
24. Z.-L. Yu, N. Yang, L.-C. Zhou, Z.-Y. Mal, Y.-B. Zhu, Y.-Y. Lu, B. Qin, W.-Y. Xing, T. Ma, S.-C. Li, H.-L. Gao, H.-A. Wu, S.-H. Yu, Bioinspired polymeric woods. *Sci. Adv.* **4**, eaat7223 (2018).
25. J. Song, C. Chen, Z. Yang, Y. Kuang, T. Li, Y. Li, H. Huang, I. Kierzewski, B. Liu, S. He, T. Gao, S. U. Yuruker, A. Gong, B. Yang, L. Hu, Highly compressible, anisotropic aerogel with aligned cellulose nanofibers. *ACS Nano* **12**, 140–147 (2018).
26. C. Chiritescu, D. G. Cahill, N. Nguyen, D. Johnson, A. Bodapati, P. Keblinski, P. Zschack, Ultralow thermal conductivity in disordered, layered WSe_2 crystals. *Science* **315**, 351–353 (2007).
27. M. D. Losego, M. E. Grady, N. R. Sottos, D. G. Cahill, P. V. Braun, Effects of chemical bonding on heat transport across interfaces. *Nat. Mater.* **11**, 502–506 (2012).
28. J.-K. Yu, S. Mitrovic, D. Tham, J. Varghese, J. R. Heath, Reduction of thermal conductivity in phononic nanomesh structures. *Nat. Nanotechnol.* **5**, 718–721 (2010).
29. G. Pernot, M. Stoffel, I. Savic, F. Pezzoli, P. Chen, G. Savelli, A. Jacquot, J. Schumann, U. Denker, I. Mönch, Ch. Deneke, O. G. Schmidt, J. M. Rampnoux, S. Wang, M. Plissonnier, A. Rastelli, S. Dilhaire, N. Mingo, Precise control of thermal conductivity at the nanoscale through individual phonon-scattering barriers. *Nat. Mater.* **9**, 491–495 (2010).
30. D. Donadio, G. Galli, Temperature dependence of the thermal conductivity of thin silicon nanowires. *Nano Lett.* **10**, 847–851 (2010).
31. L. A. Valentín, J. Betancourt, L. F. Fonseca, M. T. Pettes, L. Shi, M. Soszyński, A. Huczko, A comprehensive study of thermoelectric and transport properties of β-silicon carbide nanowires. *J. Appl. Phys.* **114**, 184301 (2013).
32. K. Zekentes, K. Rogdakis, SiC nanowires: Material and devices. *J. Phys. D Appl. Phys.* **44**, 133001 (2011).
33. G. Cheng, T.-H. Chang, Q. Qin, H. Huang, Y. Zhu, Mechanical properties of silicon carbide nanowires: Effect of size-dependent defect density. *Nano Lett.* **14**, 754–758 (2014).
34. Y. Yao, X. Zhu, X. Zeng, R. Sun, J.-B. Xu, C.-P. Wong, Vertically aligned and interconnected SiC nanowire networks leading to significantly enhanced thermal conductivity of polymer composites. *ACS Appl. Mater. Interfaces* **10**, 9669–9678 (2018).
35. H. L. Gao, L. Xu, F. Long, Z. Pan, Y. X. Du, Y. Lu, J. Ge, S. H. Yu, Macroscopic free-standing hierarchical 3D architectures assembled from silver nanowires by ice templating. *Angew. Chem. Int. Ed.* **53**, 4561–4566 (2014).
36. S. Chabi, V. G. Rocha, E. García-Tuñón, C. Ferraro, E. Saiz, Y. Xia, Y. Zhu, Ultralight, strong, three-dimensional SiC structures. *ACS Nano* **10**, 1871–1876 (2016).
37. C. Ferraro, E. Garcia-Tuñon, V. G. Rocha, S. Barg, M. D. Fariñas, T. E. G. Alvarez-Arenas, G. Sernicola, F. Giuliani, E. Saiz, Light and strong SiC networks. *Adv. Funct. Mater.* **26**, 1636–1645 (2016).
38. T. A. Schaedler, A. J. Jacobsen, A. Torrents, A. E. Sorensen, J. Lian, J. R. Greer, L. Valdevit, W. B. Carter, Ultralight metallic microlattices. *Science* **334**, 962–965 (2011).
39. Y. Si, J. Yu, X. Tang, J. Ge, B. Ding, Ultralight nanofibre-assembled cellular aerogels with superelasticity and multifunctionality. *Nat. Commun.* **5**, 5802 (2014).
40. L. R. Meza, S. Das, J. R. Greer, Strong lightweight, and recoverable three-dimensional ceramic nanolattices. *Science* **345**, 1322–1326 (2014).
41. L. J. Gibson, M. F. Ashby, *Cellular Solids: Structure and Properties* (Cambridge Univ. Press, 1997).
42. R. Lakes, Advances in negative Poisson's ratio materials. *Adv. Mater.* **5**, 293–296 (1993).
43. Q. Zhang, X. Xu, D. Lin, W. Chen, G. Xiong, Y. Yu, T. S. Fisher, H. Li, Hyperbolically patterned 3D graphene metamaterial with negative Poisson's ratio and superelasticity. *Adv. Mater.* **28**, 2229–2237 (2016).
44. C. Huang, L. Chen, Negative Poisson's ratio in modern functional materials. *Adv. Mater.* **28**, 8079–8096 (2016).
45. M. Wiener, G. Reichenauer, S. Braxmeier, F. Hemberger, H.-P. Ebert, Carbon aerogel-based high-temperature thermal insulation. *Int. J. Thermophys.* **30**, 1372–1385 (2009).

Acknowledgments: We thank C. Guo from CAMPNANO of Xi'an Jiaotong University. **Funding:** This work is supported by the foundations from the National Natural Science Foundation of China (51772237), 111 Project 2.0 (BP2018008), the Shaanxi Innovation Capacity Support Program (2018TD-031), and the Independent Innovation Capacity Improvement Plan of Xi'an

Jiaotong University (PY3A033). **Author contributions:** L.S. and H.W. conceived and designed experiments. L.S. prepared the samples. H.H., S.D., and X.P. did the TEM/STEM and EDS characterizations. L.S. did the other experiments and prepared the manuscript. All authors discussed the results and commented on the manuscript. **Competing interests:** The authors declare that they have no competing interests. **Data and materials availability:** All data needed to evaluate the conclusions in the paper are present in the paper and/or the Supplementary Materials. Additional data related to this paper may be requested from the authors.

Submitted 9 July 2019
Accepted 12 May 2020
Published 24 June 2020
10.1126/sciadv.aay6689

Citation: L. Su, H. Wang, M. Niu, S. Dai, Z. Cai, B. Yang, H. Huyan, X. Pan, Anisotropic and hierarchical SiC@SiO_2 nanowire aerogel with exceptional stiffness and stability for thermal superinsulation. *Sci. Adv.* **6**, eaay6689 (2020).